ACS APPLIED MATERIALS & INTERFACES

www.acsami.org
Research Article

Nanoengineered Osteoinductive Bioink for 3D Bioprinting Bone Tissue

David Chimene, Logan Miller, Lauren M. Cross, Manish K. Jaiswal, Irtisha Singh, and Akhilesh K. Gaharwar*

Cite This: https://dx.doi.org/10.1021/acsami.9b19037

Read Online

ACCESS | Metrics & More | Article Recommendations | Supporting Information

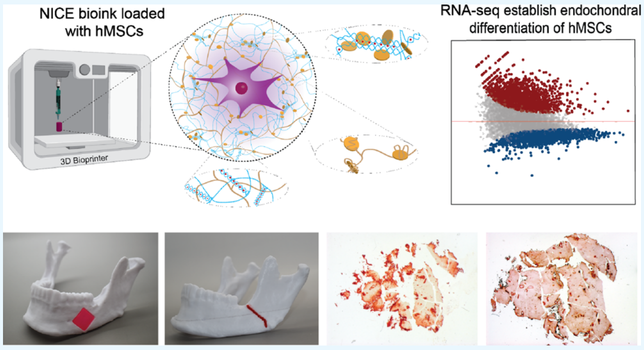

ABSTRACT: Bioprinting is an emerging additive manufacturing approach to the fabrication of patient-specific, implantable three-dimensional (3D) constructs for regenerative medicine. However, developing cell-compatible bioinks with high printability, structural stability, biodegradability, and bioactive characteristics is still a primary challenge for translating 3D bioprinting technology to preclinical and clinal models. To overcome this challenge, we developed a nanoengineered ionic covalent entanglement (NICE) bioink formulation for 3D bone bioprinting. The NICE bioinks allow precise control over printability, mechanical properties, and degradation characteristics, enabling custom 3D fabrication of mechanically resilient, cellularized structures. We demonstrate cell-induced remodeling of 3D bioprinted scaffolds over 60 days, demonstrating deposition of nascent extracellular matrix proteins. Interestingly, the bioprinted constructs induce endochondral differentiation of encapsulated human mesenchymal stem cells (hMSCs) in the absence of osteoinducing agent. Using next-generation transcriptome sequencing (RNA-seq) technology, we establish the role of nanosilicates, a bioactive component of NICE bioink, to stimulate endochondral differentiation at the transcriptome level. Overall, the osteoinductive bioink has the ability to induce formation of osteo-related mineralized extracellular matrix by encapsulated hMSCs in growth factor-free conditions. Furthermore, we demonstrate the ability of NICE bioink to fabricate patient-specific, implantable 3D scaffolds for repair of craniomaxillofacial bone defects. We envision development of this NICE bioink technology toward a realistic clinical process for 3D bioprinting patient-specific bone tissue for regenerative medicine.

KEYWORDS: *bone bioprinting, osteoinductive bioinks, nanomaterials, ionic-covalent reinforcement, hydrogels*

1. INTRODUCTION

Bioprinting is an emerging field based on layer by layer fabrication of structures containing cell-laden hydrogels, called bioinks.[1−4] The promise of precisely controlling cell and biomaterial distributions to recreate the complexity of human tissue has made bioprinting a popular research area for tissue regeneration.[5] However, the potential applications of bioprinting have been limited due to the lack of bioinks capable of meeting the demands of both three-dimensional (3D) printing and tissue engineering.[6] For example, ideal bioinks must be capable of extruding into stable 3D structures, while also protecting cells during and after printing, and providing an appropriate environment that can be remodeled into the target tissue. Unfortunately, conventional hydrogels are weak and poorly printable.[7] Compromising between these ideals has led to bioinks with subpar printability and biocompatibility, with bioinks unable to print structures taller than a few millimeters.[8] This has led to intensive research on developing bioinks that are highly printable, structurally stable, and protect encapsulated cells while facilitating long-term tissue formation.

Advanced bioinks are being developed to improve bioink mechanical properties and printability without compromising biocompatibility.[9,10] Most of the approaches to developing advanced bioinks, including interpenetrating networks and nanocomposites, work by addressing two key weaknesses of conventional hydrogel networks: stress concentrations caused by a heterogeneous network structure and poor capacity for mechanical energy dissipation. By altering hydrogel networks to reduce stress concentrations and dissipate mechanical energy under stress, mechanical performance in advanced bioinks can be dramatically improved, while maintaining a highly hydrated, biocompatible network.[9] Further, choosing reinforcement techniques that also modulate flow properties

Received: October 21, 2019
Accepted: February 24, 2020
Published: February 24, 2020

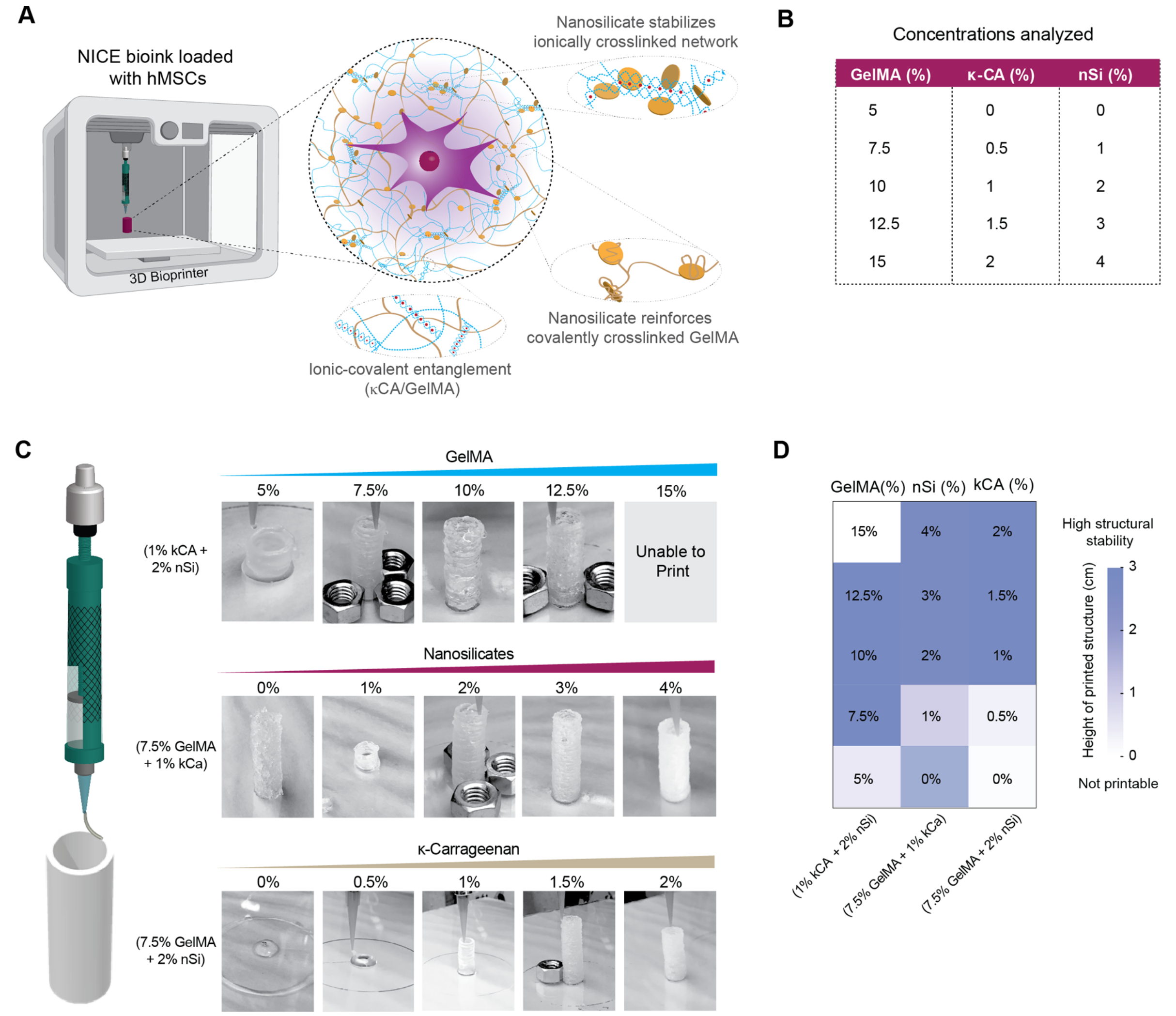

GelMA (%)	κ-CA (%)	nSi (%)
5	0	0
7.5	0.5	1
10	1	2
12.5	1.5	3
15	2	4

Figure 1. NICE bioink design and printability assessment. (A) The combination of gelatin methacrylate (GelMA), kappa-carrageenan (kCA), and nanosilicates (nSi) was used to design nanoengineered ionic-covalent entanglement (NICE) bioink. (B) Different compositions of NICE formulation was investigated . (C) The 3D printability of each NICE bioink formulation was quantified using screw-driven extrusion printer (at 37 °C) to fabricate a 3 cm tall, 1 cm wide hollow tube. The effect of different component on printability was evaluated. (D) Print success of 3D printed structure was based on the final height of the structure, conformity to expected dimensions, and lack of observable errors.

allows printability to be simultaneously enhanced. The efficiency of these reinforcement techniques is leading researchers to develop ways to combine different reinforcement mechanisms together to provide greater control over the mechanical properties and printability of bioinks.[9,10]

Here, we report nanoengineered-ionic-covalent-entanglement (NICE) bioinks as a platform technology by combining two reinforcement approaches: ionic-covalent entanglement and nanoreinforcement. To design the NICE reinforced bioinks for osteogenic tissue bioprinting, the bioink must be highly printable, be mechanically strong, induce osteogenic differentiation, and be biodegradable. The difficulty of combining these requirements into a single bioink has been a major obstacle in bioprinting since its inception. By combining these two distinct reinforcement methods, NICE reinforcement creates a robust and superior bioink while providing a highly hydrated and cell friendly microenvironment for bone bioprinting.

Both ionic-covalent entanglement and nanoreinforcement reinforce hydrogels by providing mechanisms that reversibly dissipate mechanical energy. NICE bioinks have three major components: covalently crosslinkable gelatin methacryloyl (GelMA), ionically crosslinkable kappa-carrageenan (kCA), and electrostatically charged nanosilicates (Laponite XLG, obtained from BYK Additives & Instruments). GelMA provides an extracellular matrix (ECM)-like environment that contains cell attachment sequences but is poor for bioprinting due to its thermal gelation and low viscosity. kCA is a polysaccharide obtained from seaweed that can be ionically crosslinked by potassium ions (Figure 1A, top right). This ionically crosslinked kCA network is brittle, while the covalently cross-linked GelMA network is much more elastic. The combination of GelMA and kCA results in formation of an ionic-covalent entanglement network (Figure 1A). During deformation, the ductile network (GelMA) disperses stress across a large damage zone region, while the more brittle network (kCA) is disrupted.[8] The combination of stress sharing and mechanical energy dissipation within ionic-covalent entanglement greatly increases hydrogel mechanical strength and toughness.[9,10] kCA also raises viscosity at bioprinting temperatures, preventing flow as the bioink cools.

Nanosilicates (nSi) are synthetic two-dimensional (2D) nanoclays (1−2 nm in thickness and 20−50 nm in diameter), with a positive surface charge on their faces and a negative charge around their edges.[11−13] These permanent surface charges allow the nanoparticles to form noncovalent electrostatic bonds with polymers (GelMA and kCA). These bonds act as weak reversible crosslinks to dissipate mechanical energy without disrupting the hydrogel's overall network structure, reinforcing the hydrogel.[6,9] These same interactions also give nanosilicates powerful effects on flow behavior that can be exploited to simultaneously improve printability. Nanosilicate-polymer solutions are highly shear thinning but have heightened viscosity at low shear.[8] This allows apparent viscosity to drop as the ink flows through the extruder tip, protecting cells, but quickly rise after extrusion, which keeps the extruded bioink in place.

The addition of nanosilicates incorporates osteogenic properties to NICE bioink. Our earlier studies have demonstrated that nanosilicates can induce osteogenic differentiation of hMSCs in absence of osteoinductive agents, such as dexamethasone or bone morphogenic protein-2 (BMP-2).[14,15] Interestingly, the osteoinductive ability of nanosilicates is retained when added to polymeric hydrogels.[16,17] Using whole transcriptome sequencing (RNA-seq) we evaluated that nanosilicates induce endochondral differentiation of stem cells.[15] In addition, the charged characteristics of nanosilicates can sequester endogenous or exogenous biomolecules, which can be used to modulate cellular functions.[11−13,18] On the basis these studies, it is expected that addition of nanosilicates to NICE bioink can induce osteogenic differentiation of bioprinted cells in absence of osteoinductive agents such as dexamethasone or BMP-2.

The development of the osteoinductive NICE bioink followed several steps. First, a range of bioink formulations were developed and tested for printability performance and rheological properties. The selected bioink was used to bioprinted scaffolds to demonstrate potential clinical uses. Next, the mechanical and degradation characteristics of the most suitable bioinks are evaluated. Finally, human mesenchymal stem cells (hMSCs) were encapsulated in the bioink and bioprinted into 3D scaffolds. These cell-laden 3D printed structures were evaluated over a long term (~60 days) under osteoconductive culture conditions (in absence of osteoinductive agents). The histological changes related to tissue remodeling as well as calcium deposition were monitored to evaluate the osteogenic differentiation of encapsulated cells.

2. RESULTS AND DISCUSSION

2.1. Designing Bioink and Optimizing its Printability and Performance. Many existing bioinks are capable of printing small structures with a few millimeters tall due to their flow characteristics. However, for bioinks to be used for bone regeneration, they must be able to precisely replicate large, centimeter scale bone segments that may be irregularly shaped in all three dimensions. Therefore, optimized bioinks must be first evaluated for printability. We elected to start with a NICE formula established to be able to print tall, high aspect ratio structures to find a range of printable compositions (Figure 1B). Each composition was printed into a standard test cylinder, where a 3 cm (150 layer) tall, hollow cylinder was printed, with a 10 mm outer diameter and 1 mm thick walls (Figure 1C). The printability performance was quantified by determining (1) whether a composition could reach the full 3 cm height, (2) the absence of major defects by testing whether the cylinder could hold water and (3) fidelity between the height and diameter of the printed cylinder and its intended dimensions.

Initial testing focused on varying GelMA concentration from 5 to 15% while holding kCA (1%) and nSi (2%) concentrations constant (Figure 1C, top row). The bioink with the lowest amount of GelMA (5% GelMA, 1% kCA, 2% nSi) sagged under its own weight and could not be printed above 1 cm in height, while higher amounts of GelMA (7.5−12.5%) bioinks were able to print to 3 cm tall cylinders. The observed sagging in 5% GelMA composition is attributed to its reduced viscosity and lower thermal gelation. 7.5% GelMA concentrations were printed without any visible wall defects, while higher GelMA concentrations were more prone to defects caused by nozzle clogging. Increasing GelMA concentrations led to more rigid cylinders. These observations were attributed to stronger and more rapid thermal gelation at higher GelMA concentrations. When the GelMA concentration was raised to 15%, rapid changes in viscosity during printing caused extensive clogging, making printing difficult. These observations suggest that GelMA's thermal gelation plays a role analogous to cooling in thermoplastic printing: thermal gelation stabilizes extruded filament during printing, so insufficient gelation causes structures to "melt", while too much gelation causes clogging and reduces interlayer adhesion.

The NICE bioink composition with 7.5% GelMA, 1% kCA, and 2% nSi was the most printable, so it was used as the basis for testing nanosilicate concentration (Figure 1C, middle row). Nanosilicates imbue bioinks with shear thinning behavior, which has been shown to improve printability by reducing apparent viscosity during extrusion. Interestingly, the bioink was able to reach[11] the full 3 cm height with 0% nanosilicates but was plagued with major errors and holes throughout the print caused by inconsistent extrusion and high self-adhesion. Furthermore, addition of 1% nSi brought smoother extrusion but actually decreased the maximum height by reducing the amount of self-adhesion shown by the bioink. In contrast, printing with 2, 3, and 4% nSi concentrations led to smooth, consistently extruded cylinders. Because the print quality was substantially equivalent at these concentrations, the 2% nSi NICE formulation was selected for future studies.

Finally, printability was tested at kCA compositions (0, 1, and 2%) (Figure 1C, bottom row). At 0 and 0.5% kCA concentration, bioinks were not viscous enough to hold their shape and could not be printed above a few millimeters. Bioink containing 1, 1.5, and 2% kCA were able to print structures 3 cm high and were free of structural defects. These observations suggest that without sufficient kCA, GelMA and nSi print poorly because they flow extensively before thermal gelation (Figure 1D). kCA provides the critical viscosity and yield stress needed to hold extruded layers in place while they cool and solidify through thermal gelation.

2.2. Rheological Characteristics of NICE Bioinks. Small changes in bioink composition yielded significant changes in printability, so key flow properties of each bioink were examined to investigate the rheological characteristics necessary for good printability. Printing performance suggested a relationship between thermal gelation and print performance, so peak hold rheology tests were designed to simulate bioink's environment during the 3D printing process. In this peak hold test, the bioink is subjected to three stages designed to replicate the conditions of the bioink during printing: a pre-

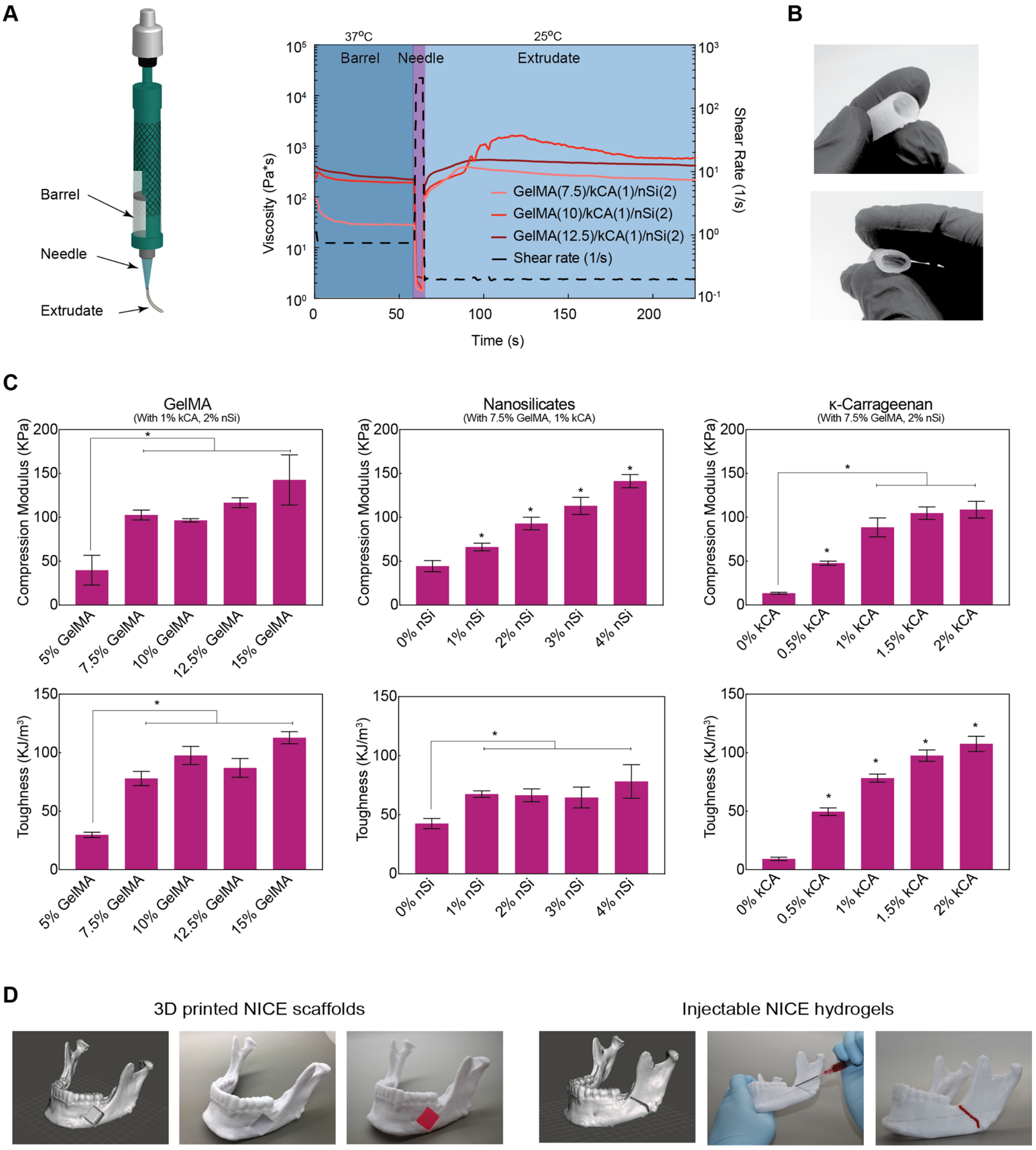

Figure 2. Rheology of the NICE bioink and mechanical performance of 3D printing structures. (A) Shear recovery tests showed that print performance corresponds well with rapid viscosity recovery, which reaches over 100% recovery due to thermal gelation. (B) NICE printed structures (7.5% GelMA, 1% kCA, 2% nanosilicates) are highly flexible and resilient. 3D printed tube structures (3 cm in height) can be completely collapsed and quickly regain their shape. (C) Mechanical testing showed that increase in the concentration of polymer and nanoparticles improves mechanical stiffness and toughness of 3D printed structures (100% infill density). (D) The NICE bioink can be printed into custom scaffolds or can be injected into the defect site.

extrusion phase, an extrusion phase, and a postextrusion phase (Figure 2A). The pre-extrusion phase is kept at 37 °C and uses a very low shear rate ($1\ s^{-1}$) corresponding to shear conditions in the barrel, followed by a 5 s high shear rate ($300\ s^{-1}$) phase simulating extrusion. The bioink was then quickly cooled to 25 °C and held at a minimum shear rate ($0.2\ s^{-1}$) representing the postextrusion phase. We calculated shear rate at the extruder tip walls, which was used for the high shear rate. The entire test was carried out at 200 μm sample height, corresponding to the internal radius of the extruder tip. By matching the physical conditions found during printing as closely as possible, we can measure the rate and extent of thermal gelation through changes in apparent viscosity and observe shear thinning in action.

GelMA is the biggest contributor to thermal gelation, and peak hold experimental data is shown for the varied GelMA compositions (Figure 2A). Peak hold tests show that apparent viscosity drops by several orders of magnitude during the high shear rate extrusion phase, then rapidly recovers within just a couple of seconds post extrusion. Apparent viscosity then continues to increase steadily over roughly 30 s due to thermal gelation, as viscosity recovery exceeds 200−1000% of its pre-extrusion value. Matching up with printability observations, increasing GelMA concentration increases initial viscosity and viscosity recovery speed, although the final viscosity of the 10% GelMA NICE was somewhat higher than the 12.5% composition. The NICE bioink with 7.5% GelMA was notably less viscous at 37 °C than the 10 and 12.5% formulations before and during extrusion, which explains the observed smoother printed structures. This explains the ability to create strong, many-layered structures. Previous studies have highlighted the importance of dramatic shear thinning followed by rapid shear recovery as key to bioink printability, and the rheology data shown here for the highest performing bioinks fits well into this paradigm.[8,19]

2.3. Mechanically Stiff and Elastomeric 3D Printed Scaffolds. A bioink's mechanical properties are key to its performance in tissue engineering. The stiffness of the extracellular environment plays a critical role in regulating cell proliferation, migration, and differentiation.[20] Human mesenchymal stem cells (hMSCs) sense and interact with their environment through an array of cytoskeletal and membrane proteins, allowing them to differentiate into appropriate body tissue based on their surroundings.[21] For example, stiffer ECM environments at least 25−40 kPa match the stiffness of osteoid tissue produced during initial bone healing, and direct hMSCs toward an osteogenic lineage.[22] GelMA-nSi nanocomposites similar to the NICE bioink have been shown to induce osteogenic differentiation without exogenous osteoinductive factors.[17,23] Beyond cell interactions, bioprinted structures must be strong enough to handle manipulation and implantation during surgery, and be resilient enough to maintain their integrity during neo-tissue formation.

In light of these requirements, the mechanical properties of 3D printable hydrogels were investigated. The crosslinked 3D printed hydrogels were able to sustain mechanical deformation, such as shearing, bending, and stretching, without apparent permanent deformation and rapidly recovered their original shape (Figure 2B). Single cyclic compression cycles to 70% compression (unconstrained) were carried out on 3D printed structure with 100% infill. The compressive modulus and toughness were calculated. As in the printability investigation, the hydrogels were based off of a standard formula (7.5% GelMA, 1% kCA, 2% nSi) and a single component was varied at a time. Compression modulus data (Figure 2C, top) showed that at the lowest GelMA concentration (5%), the compressive modulus was 40 ± 17 kPa, while at 7.5% GelMA the stiffness significantly increased to 103 ± 6 kPa. Increasing GelMA concentration above 7.5% did not significantly increase the modulus. The toughness of the gels also showed similar trends with significant increase from 5 to 7.5% GelMA concentration (30 ± 2 and 78 ± 6 kJ/m^3, respectively). Further increases in GelMA concentration did not significantly improve toughness (Figure 2C, bottom). In contrast, stiffness increased steadily and significantly with increasing nanosilicate concentration between 0 and 4% (44 ± 6 up to 141 ± 8 kPa). Interestingly, while the addition of nanosilicates increased toughness (42 ± 4 kJ/m^3 at 0% to 67 ± 3 kJ/m^3 at 1%), further increases in nSi concentrations did not have a significant effect. Both compressive modulus and toughness trended significantly upward as kCA content increased (13 ± 1 kPa and 9 ± 1 kJ/m^3 at 0% up to 109 ± 10 kPa and 108 ± 7 kJ/m^3 at 2%). However, diminishing returns were clearly evident past 1% kCA.

Together, this data shows that each reinforcement mechanism leads to significant increases in stiffness and toughness. Nanosilicates steadily increase stiffness but not toughness past 1%, while kCA increases both stiffness and toughness although returns from additional polymer seem to diminish quickly. 7.5% GelMA was also established as a minimum requirement for both compressive modulus and toughness. Since a highly hydrated and easily remodelable bioink is desired, establishing relationships between composition and mechanical properties allows us to find the lowest polymer and nanomaterial concentrations needed to create mechanically robust bioinks. In combination with the printability performance data, these mechanical results allowed us to identify an optimal bioink for osteogenic testing and illustrates the dual roles played by the three primary bioink components in both mechanical properties and printability.

To illustrate the practical utility of NICE bioinks for bone tissue reconstruction, we demonstrate how to create full-scale bioprinted implants customized for craniofacial defects on real patient CT scans. Publicly available DICOM files were downloaded and converted into an anonymized file. The NRRD file using an open-source slicer program was then converted into an.STL file with the Democratiz3d tool available online. Meshmixer was used to process the models and create bone defects, and slic3rPE and Repetier Host were used to bioprint the scaffolds. This process uses entirely open-source or free software. After bioprinting, the scaffold was crosslinked and implanted in a thermoplastic model of the mandible to demonstrate the closeness of fit (Figure 2D). The defect in the mandible is 2 × 2 × 1 cm^3. The potential for using the NICE bioink as an injectable material in smaller defects was also investigated, showing that the bioink injects easily through an 18-gauge needle into a simulated fracture, and can be rapidly crosslinked in place using 60 s of 365 nm light and 0.25% Irgacure 2959 as a photoinitiator. Strength of fit was also demonstrated by injecting and crosslinking the NICE bioink between two sections of a full thickness fracture to demonstrate that the NICE bioink is able to quickly adhere surfaces together and resist shearing and delamination forces.

In light of these results, a final bioink concentration of 7.5% GelMA, 2% Nanosilicates, and 1% kCA was selected as the optimized bioink to be tested going forward. This composition contains the minimum polymer and nanoparticle content needed for excellent printability and exceeds the established modulus requirements for osteogenic differentiation by a comfortable margin. Therefore, this NICE bioink represents the essential composition needed to both exhibit good mechanical properties and be highly printable.

2.4. Cell-Assisted Matrix Remodeling of 3D Printed Structure. The ability of cells to remodel their microenvironment by degrading their surroundings to grow and deposit ECM has led to expanded interest in designing biodegradable inks. Enzymatically degradable bioinks are especially attractive for 3D bioprinting because they mimic the ability of native tissue to degrade in response to cell signaling. The covalently crosslinked GelMA network of NICE bioinks is susceptible to enzymatic (collagenase) degradation. The degradation rate is a critical factor in successful tissue regeneration: too rapid a degradation will cause a scaffold to degrade faster than tissue can be formed to replace it, while excessively slow degradation will retard growth and healing. To get a baseline estimate of the degradation profile of NICE bioink, samples were printed and incubated under cell culture conditions in phosphate buffered saline (PBS), osteoconductive media, or media with collagenase (300 u/mL). The osteoconductive media contains ascorbic acid and β-glycerophosphate but no osteoinductive

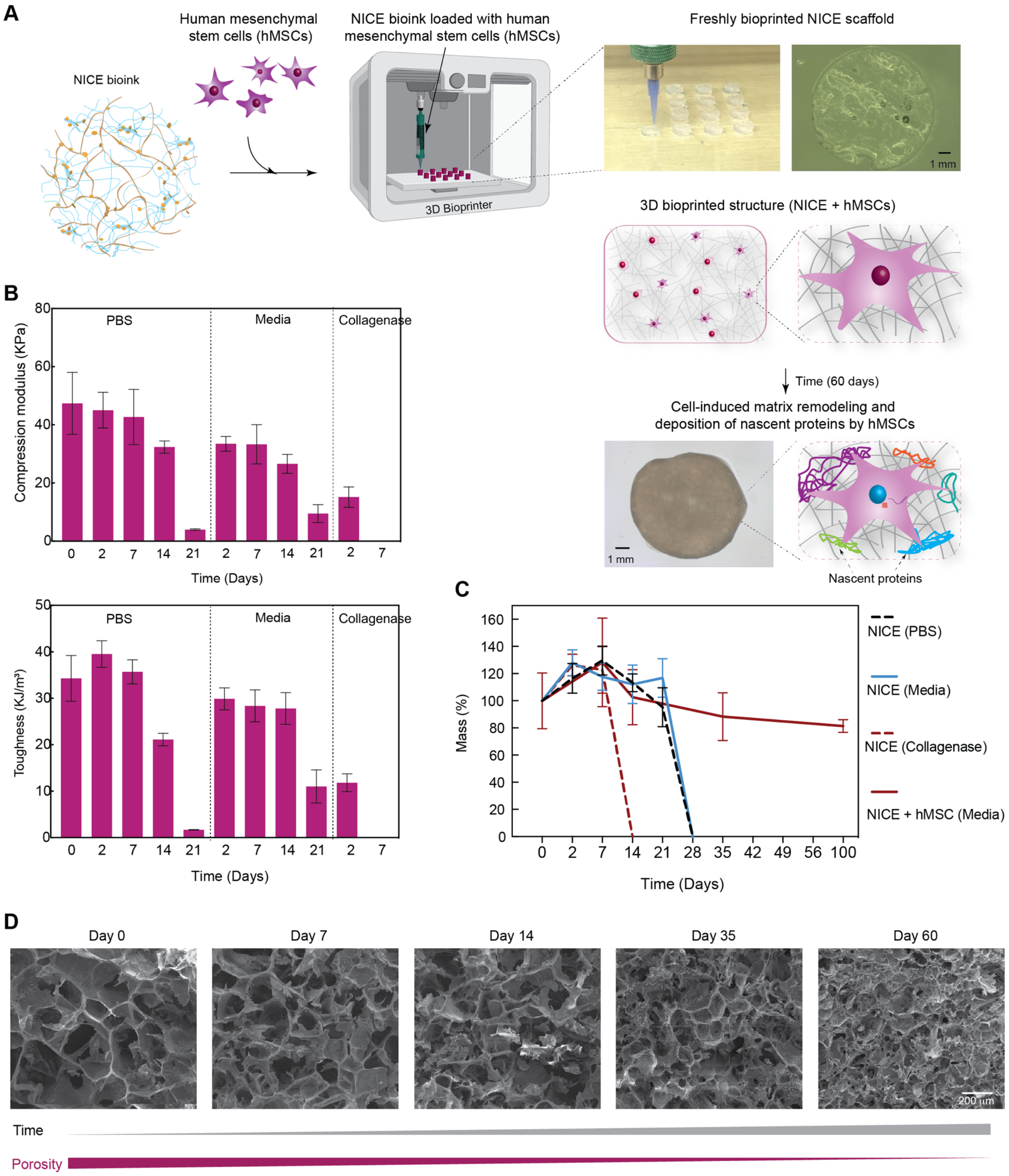

Figure 3. 3D bioprintedNICE scaffolds support cell-induced matrix remodeling. (A) hMSCs are encapsulated in the NICE bioink and cell-laden scaffolds are printed ($n = 5$). Initially the scaffolds are transparent but the scaffolds turn translucent due to remodeling and deposition of nascent proteins after 60 days. The matrix remodeling in presence of cells is monitored by determining (B) mechanical stability and (C) scaffold mass in PBS, media, and collagenase. Three-dimensional printed scaffolds completely degrade in PBS and media within 4 weeks. The presence of collagenase degrades the scaffolds within 2 weeks. For bioprinted scaffolds (loaded with hMSCs), no significant mass loss was observed even after 100 days of cultures. This indicates that matrix deposition by cells is able to keep the structure intact. (D) Scanning electron microscopy (SEM) images taken at different times show gradual changes in the microstructure of cell-containing 3D bioprinted scaffolds. Over time, a decrease in pore size was observed due to deposition of ECM by cells.

factors such as dexamethasone or BMP-2. We selected osteoconductive media to demonstrate the osteoinductive ability of NICE bioink.

Initially, 3D bioprinted scaffolds were transparent, but after culturing for 60 days, the scaffolds become opaque (Figure 3A). It is expected that such change in optical properties might be attributed to cell-induced matrix remodeling and deposition of nascent proteins. To determine cell-assisted matrix remodeling, 3D printed samples were mechanically tested to measure changes in mechanical properties and weighed for mass loss. Cell-containing bioinks were also printed and cultured, then imaged with a scanning electron microscope to investigate changes in microstructure.

Mechanical testing revealed that the 3D printed scaffolds subjected to PBS and media maintained their compression modulus and toughness for 14 days but suffered significant

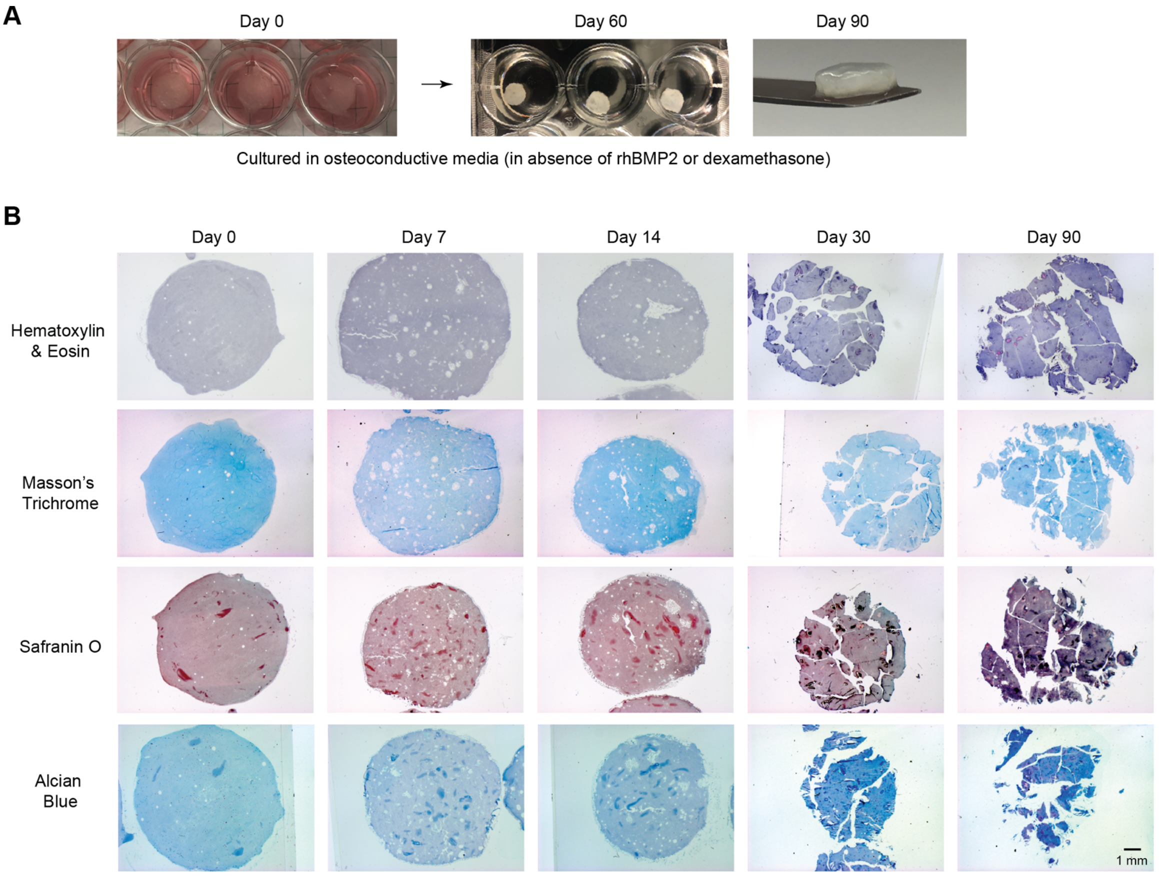

Figure 4. Extracellular matrix (ECM) remodeling in 3D bioprinted scaffolds. (A) Bioprinted structures are initially (day 0) transparent but become opaque over time (day 60) due to cell-induced matrix remodeling and deposition of mineralized matrix. (B) Histology show progressive changes in the ECM of 3D bioprinted structures. Safranin O stains cartilage tissue in varying shades of red, while bone tissue is bluish-purple. Alcian Blue stains connective tissue light blue and cartilage dark blue. Together, these stains demonstrate the osteochondral production of cartilage ECM that transitions into mineralization. In osteochondral tissue formation, hMSCs differentiate into osteochondral progenitor cells and then into chondrocytes, producing a cartilaginous extracellular matrix. Chondrocytes then differentiate into preosteoblasts and direct the mineralization of the surrounding matrix.

losses by day 21 (Figure 3B). For example, a 5- and 10-fold reduction in the mechanical modulus was in media (9.5 ± 3 kPa) and PBS (4 ± 0.25 kPa) after 21 days, compared with the initial modulus of scaffolds (47 ± 10 kPa) on day 0. In contrast, samples subjected to collagenase were partially degraded by day 2 (15 ± 7 kPa) and completely degraded by day 7. Mass loss data showed that 3D printed structures swelled roughly 20% mass in the first week of culture, but otherwise did not significantly lose mass through day 21. By 28 days, the non-cell containing scaffolds were fragmented into pieces too small to measure. This data indicates that the scaffolds maintain their mechanical properties for at least 2 weeks, and their overall mass, for at least 3 weeks. In addition, the printed scaffolds are sensitive to enzymatic degradation despite the presence of a secondary ionic network. The lower starting values relative to mechanical data are to be expected, since bioprinted scaffolds swell and are not perfectly flat, which affects mechanical property measurements, and no delamination was observed during mechanical testing. Importantly, bioprinted (cell-containing) scaffolds show very different behavior compared with scaffolds without cells. Bioprinted scaffolds retained their structural integrity and preserved over 80% of initial mass up to 60 days (Figure 3C). SEM imaging reveals increased microstructure density starting after day 14 (Figure 3D). This suggests that substantial cell-mediated remodeling occurs that is extensive enough to hold together the macroscopic structure of 3D printed scaffolds.

Overall, this in vitro biodegradability data gives us an estimated window of biodegradation that is useful for evaluating a bioink, but they are difficult to correlate to results in vivo. This is because degradation in vivo can vary widely based on immune response and extent of tissue ingrowth, and collagenase levels change by orders of magnitude based on inflammatory reactions. Using a supraphysiological collagenase concentration allows us to establish a lower limit for structural integrity. However, tissue in-growth may also be much more rapid in vivo due to better nutrient transfer.

2.5. Deposition of Nascent Extracellular Matrix. The extracellular matrix (ECM) surrounding cells plays a key role in the development of functional tissue. The properties of the ECM are critical factors in cell adhesion, motility, migration, differentiation, and proliferation. In addition, recent studies have shown that encapsulated cells can remodel polymeric network by depositing nascent protein that dictate fate of cells.[24] Thus, determining how bioprinted cells interact with and remodel their microenvironment allows us to understand how bioprinted implants behave in vitro and gives us insight into what we can expect under in vivo conditions.[25,26]

Our earlier studies established the role of nanosilicates in directly stimulating hMSCs toward endochondral differ-

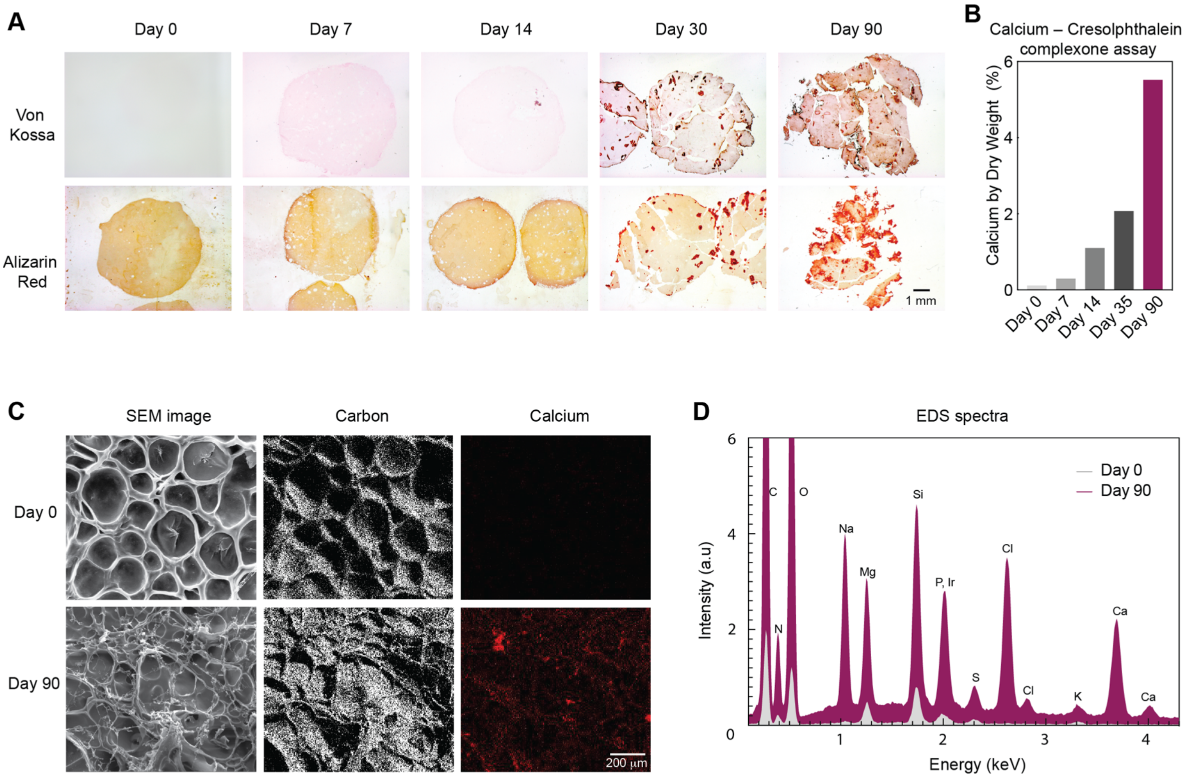

Figure 5. Mineralized matrix in 3D bioprinted scaffolds. (A) The presence of mineralized ECM in 3D bioprinted scaffolds over a course of 90 days was determined using Von Kossa and Alizarin Red staining. (B) A calcium-cresolphthalein complexone assay was used to quantify the amount of calcium in the 3D bioprinted scaffolds over time. (C) SEM−energy dispersive spectroscopy (EDS) imaging was used to visualizes the increase in calcium content over time in the 3D bioprinted scaffold. (D) EDS quantitative data shows an increase in calcium and phosphates content after 60 days of culture due to osteogenic differentiation of hMSCs.

entiation in growth-factor-free culture conditions.[15] The addition of nanosilicates to polymeric networks such as GelMA have shown to preserve the osteoinductive ability of nanosilicates in the absence of osteoinductive agents.[16,17] On the basis of these studies, it is expected that NICE bioprinted scaffolds will induce endochondral differentiation of encapsulated hMSCs in osteoconductive media (in absence of dexamethasone or BMP-2). We investigated this by evaluating the production of cartilage-rich ECM that is subsequently calcified to form a mineralized matrix.

We used histology to evaluate remodeling of NICE bioprinted scaffolds by hMSCs over several months, showing an endochondral ossification-like remodeling process of cartilage formation followed by mineralization that resembles natural bone formation. The persistence of cell-containing scaffolds beyond 4 weeks suggests that the encapsulated cells remodel the scaffolds over time. To investigate ECM deposition by the hMSCs, cell-containing scaffolds were 3D bioprinted and cultured for 60 days and histologically examined at regular time points (0, 7, 14, 30, and 90 days). As observed under a simple light microscope, scaffolds were initially transparent on day 0 and gradually became translucent and pearlescent over by day 60 (Figure 4A). mRNA extraction was also performed but was unsuccessful due to the charged nature of the nanosilicates interfering with mRNA extraction from the 3D encapsulated cells. However, histology still allows us insight into cell behavior through characterizing ECM deposition. Osteoblasts formed from hMSCs will produce an osteoid-like matrix, composed of collagen I and glycosaminoglycans (GAGs) including chondroitin and keratan sulfate, and two chief glycoproteins, osteocalcin and sialoprotein. The deposition of these proteins should facilitate formation of bonelike ECM either directly or through an intermediate cartilage state also known as endochondral ossification.[27] The histological staining performed here are based on identifying osteoid and cartilage-like features and establishing calcium deposition (Figure 4B). Note that bioprinted scaffolds remained intact throughout the culture period and that fractures shown on histology images are due to sample processing.

Safranin O is a cationic stain that electrostatically binds to glycosaminoglycans (large, negatively charged polysaccharides that modify osmotic pressure and diffusion rate), which are found in both osteoid and cartilage ECM. Between day 0 and 14, increasing vivid red staining indicates an increased GAG content throughout the scaffold. Past day 14, the scaffolds progressively darken to a deep bluish purple, indicating the progressive development of bonelike tissue in culture. Alcian blue, which stains proteoglycans, dyes both cartilage and osteoid a deep blue. Staining is observed to increase steadily throughout culture, including in areas of bonelike tissue as indicated by safranin O.

Masson's trichrome was used as an auxiliary test to differentiate between bone and cartilage ECM, since bone is stained a dark blue while cartilage remains a pale blue. When compared with safranin O staining, light and dark blue patterns correspond to the bone and small cartilage regions seen in Safranin O staining, further indicating that these observed regions are deposited osteoid-like and cartilage regions.

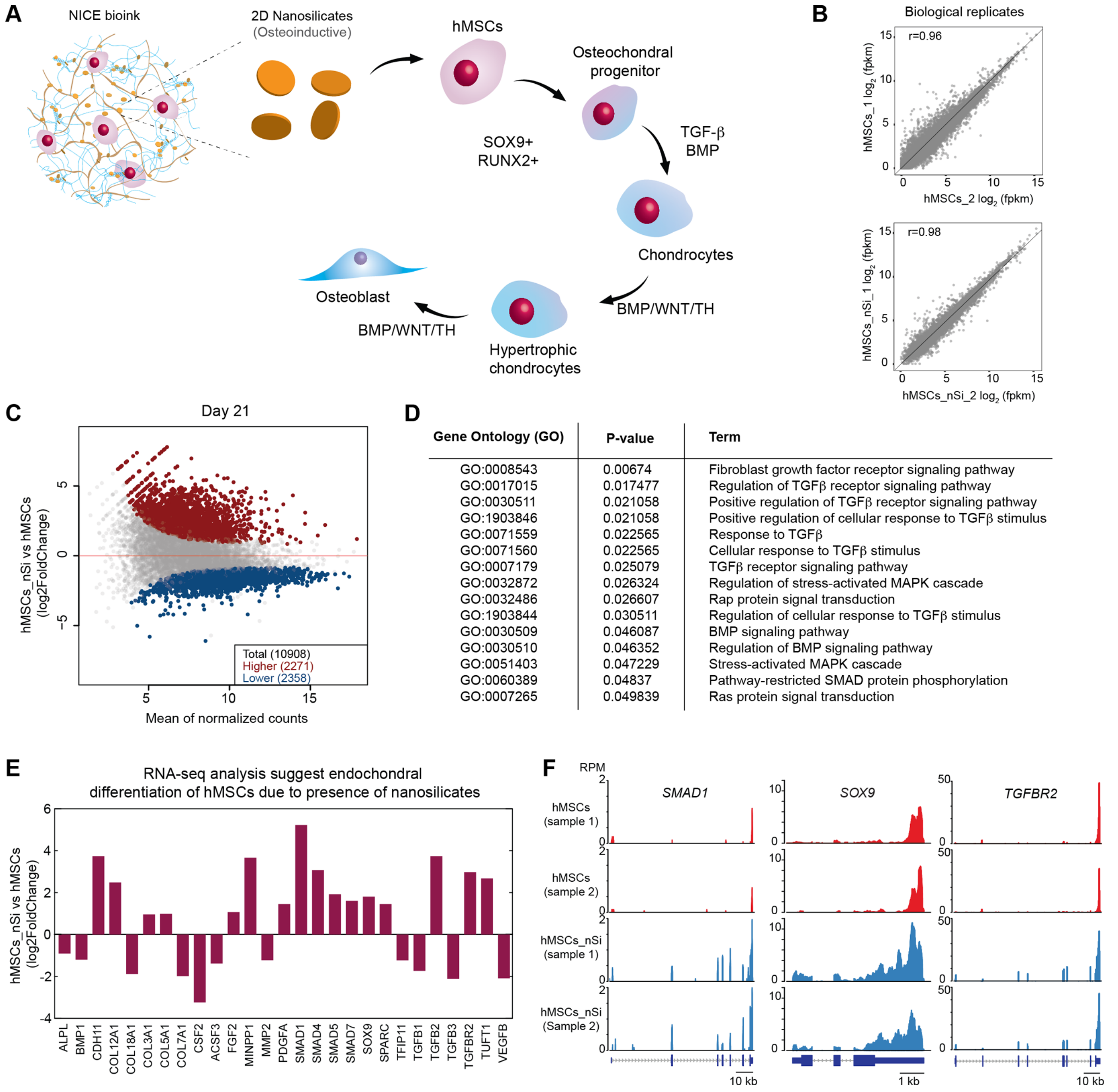

Gene Ontology (GO)	P-value	Term
GO:0008543	0.00674	Fibroblast growth factor receptor signaling pathway
GO:0017015	0.017477	Regulation of TGFβ receptor signaling pathway
GO:0030511	0.021058	Positive regulation of TGFβ receptor signaling pathway
GO:1903846	0.021058	Positive regulation of cellular response to TGFβ stimulus
GO:0071559	0.022565	Response to TGFβ
GO:0071560	0.022565	Cellular response to TGFβ stimulus
GO:0007179	0.025079	TGFβ receptor signaling pathway
GO:0032872	0.026324	Regulation of stress-activated MAPK cascade
GO:0032486	0.026607	Rap protein signal transduction
GO:1903844	0.030511	Regulation of cellular response to TGFβ stimulus
GO:0030509	0.046087	BMP signaling pathway
GO:0030510	0.046352	Regulation of BMP signaling pathway
GO:0051403	0.047229	Stress-activated MAPK cascade
GO:0060389	0.04837	Pathway-restricted SMAD protein phosphorylation
GO:0007265	0.049839	Ras protein signal transduction

Figure 6. Changes in hMSC gene expression in response to nanosilicates after 21 days of culture. (A) We can investigate the effects of nanosilicates on the gene expression profile by subjecting hMSCs to nanosilicates (in absence of any growth factors) for 21 days. hMSCs differentiate down an osteochondral pathway by SOX9 gene expression and interplay between morphogenetic signaling molecules (including TGF-β and BMP) mediates between chondrogenic and osteogenic cell behavior. (B) High correlation between two replicates for hMSCs control ($r = 0.96$) and hMSCs treated with nanosilicates (hMSCs_nSi) ($r = 0.98$). (C) Differential gene expression analysis revealed large number of genes to be either up- (red, $n = 2271$) or down- (blue, $n = 2358$) regulated due to nanosilicates treatment. (D) Gene ontology (GO) analysis of DEGs are enriched in multiple signaling pathway . (E) Fold-change in expression of selected DEGs (due to nanosilicate treatment) that are known to play important role in endochondral differentiation are shown. (F) Gene tracks of *SMAD1*, *SOX9*, and *TGFBR2* showing the expression in different samples.

Together, these histological evaluations demonstrate that the 3D bioprinted scaffolds are extensively remodeled by encapsulated hMSCs, which create a cartilage and osteoid-like ECM that is mineralized over time (Figure 4B). This shows that the optimized NICE bioink is able to induce osteogenic differentiation and tissue remodeling, even in the absence of osteoinductive factors. Further, the scaffolds maintain their overall shape and integrity during this several month incubation and remodeling, which suggests that the scaffold's biodegradation is timed well with cellular remodeling.

2.6. Evaluation of Matrix Mineralization.

To differentiate between osteoid and actual calcified bone, Von Kossa and Alizarin red stains were marked (Figure 5A). Alizarin forms an orange-red chelation complex with calcium, while Von Kossa staining precipitates silver on phosphate groups in bone, replacing calcium in the phosphate-calcium complex. Both of these stains indicate the presence of osteogenic mineralization. As expected, neither Von Kossa nor Alizarin red show significant presence of calcium or phosphates in early time points, but after several weeks, significant calcium and phosphate deposition is seen.

https://dx.doi.org/10.1021/acsami.9b19037

Calcium content was quantified using a calcium-cresolphthalein complexone assay (Figure 5B). This assay forms a vivid purple complex with elemental calcium, which can be analyzed using a spectrophotometer to precisely quantify the overall concentrations of calcium in each sample. Calcium content increased steadily from undetectable at day 0 to 1.6 ± 0.3% at 30 days, then calcium deposition increased rapidly to 5.5 ± 1% total scaffold weight by day 60. This accelerated calcium deposition in the second is consistent with the calcification of increasingly available phosphate containing, bonelike ECM, as shown by our histology data.

To better understand the mineralization occurring in the scaffolds, scanning electron microscopy energy dispersive spectroscopy (SEM−EDS) was performed. SEM−EDS uses X-rays to eject inner-shell electrons from sample material and records the characteristic energy of photons emitted when an outer shell electron fills the vacancy. Because the energy of emitted photons is element specific, peaks in the X-ray spectra identify the elements present and their relative proportions. Visualization of element presence is detected by EDS (Figure 5C). Initial EDS scans show the presence of carbon and no detectable calcium, as expected, while the 60 day culture shows calcium deposition throughout the scaffold. This elemental analysis confirms the presence of calcium deposition during culture. Quantitative comparison of X-ray spectra between the bare NICE hydrogel and a bioprinted scaffold after 60 days of culture also showed significant differences (Figure 5D). Cultured scaffolds showed large, new peaks for phosphorous and calcium, as would be expected for new hydroxyapatite formation. Relative peak heights indicate a 0.83 Ca/P ratio, while mature bone is closer to 1.68 Ca/P, with almost exactly half of the expected calcium present. This ratio suggests that calcium deficient hydroxyapatite is being formed, which may be due to the artificially limited calcium available from media. However, sample roughness can significantly distort X-ray EDS data so the highly porous lyophilized scaffolds may interfere with the quantitative analysis. Alternatively, a silicate substituted calcium-phosphate may have formed.[28]

2.7. Establishing the Role of Nanosilicates in Endochondral Differentiation. To confirm endochondral bone formation, we used RNA whole-transcriptome sequencing to characterize the gene expression in our hMSCs (Figure 6A). Because highly charged nanosilicates in the NICE bioink interfered with sufficient RNA extraction from encapsulated hMSCs, we instead opted to evaluate the effects of nanosilicates on hMSCs directly under 2D culture conditions. Specifically, hMSCs were exposed to nanosilicates (50 μg/mL) on day 0 and then cultured in osteoconductive media (in the absence of osteoinductive agents such as dexamethasone or rhBMP2) for 21 days. mRNA was isolated and whole transcriptome sequencing (RNA-seq) was performed to determine the effects of long-term nanosilicate exposure on hMSCs. The high-throughput sequencing of expressed transcripts (RNA-seq) provides an accurate quantification of expressed transcripts by overcoming the limitations and biases of microarrays.[29−31] The biological replicates for both conditions showed high concordance (r = 0.96 and r = 0.98 between replicates of hMSCs and hMSCs treated with nanosilicates, respectively) (Figure 6B). Generalized linear models (GLMs) were used to determine differentially expressed genes (DEGs) between nanosilicate treated hMSCs and untreated hMSCs. Significant changes were seen in the expression levels of 4629 genes (2271 upregulated genes, 2358 downregulated genes, FDR-adjusted $p< 0.01$) out of ∼10 908 expressed genes defined by criteria (see Method section) on day 21 (Figure 6C).

Gene ontology (GO) analysis of DEGs are enriched in key signaling pathways involved in endochondral differentiation, including fibroblast growth factor (FGF) signaling pathway, transforming growth factor β (TGF-β) signaling pathway, stress-activated protein kinase signaling cascade such as Mitogen-activated protein kinase (MAPK), as well as bone morphogenic protein (BMP) signaling pathway (Figure 6D). A range of well established genes involved in endochondral differentiation of hMSCs are upregulated due to nanosilicates treatment, including *COL1A21*, *SMAD1/4/5/7*, and *SOX9* (Figure 6E). It is well established that during chondrogenesis, *SOX9* which a master transcription factor, is upregulated .[32] In addition, expression of essential genes involved during the osteoblast development, including *TGF-β 2* and the *TGF-β 2* receptor, were also upregulated due to nanosilicate treatment . TGF-β is shown to plays important roles in osteoblast differentiation and ECM production during bone formation.[33,34] Important gene involved in BMP signaling pathways was also affected, including *BMP1*, *BMP4*, and *BMP2K*. *FGF*, which promotes osteoblast differentiation, was upregulated as well.[33]

The SMAD protein family, which acts as the main transduction pathways for BMP and TGF signaling, was also upregulated.[33] Both BMP and TGF signaling factors activate SMAD signaling pathways, with SMAD 1 and 5 mediating BMP signaling and *SMAD* 2 and *SMAD* 3 mediating TGF. *SMAD 4* is a co-SMAD for both signal pathways, while *SMAD 7* inhibits both TGF and BMP signaling. We observed significantly increased expression of *SMADs 1/4/5/7*, suggesting that BMP signaling was utilizing the SMAD pathway to mediate osteogenic behavior in bioprinted cells. Finally, osteoblast-expressed genes were also observed. Osteonectin (*SPARC*) expression, which is necessary for collagen mineralization in bone, was significantly increased. We also observed increased expression of cadherin-11, which is associated with osteoblast differentiation.

Overall, whole-transcriptome sequencing of hMSCs exposed to nanosilicates allowed us to identify increased gene expression indicating endochondral bone formation. Notably, both BMP and TGF signaling were present along with increased expression of their SMAD signaling pathways. Genes expressed in cartilage and bone were present at day 21, supporting our histology data showing that the NICE bioink induces endochondral differentiation in bioprinted hMSCs. Future studies will expand on this whole-transcriptome sequencing to more fully characterize hMSC responses to the nanosilicate containing NICE bioinks.

3. CONCLUSIONS

We introduce a NICE bioink formulation with multiple desirable characteristics for 3D bioprinting bone tissue including high print performance, enzymatic degradability, and osteoinductivity . First, we optimized an enzymatically degradable bioink to maximize printability and mechanical properties. Then, bioink remodeling was established using degradation tests and followed over 3 months (90 days) with a series of histological examinations of cell-laden 3D bioprinted scaffolds. These tests established that cells deposit a cartilage/osteoid-like matrix of GAGs, collagen, and proteoglycans over the initial few weeks of culture, followed by extended mineralization with carbonates, phosphates, and calcium. These results are supported further by SEM−EDS data and calcium assays. We also evaluated the response of hMSCs to nanosilicate, whole transcriptome sequencing was used to identify potential signaling pathways. This data suggest that observed bone tissue formation is resulting from endochondral differentiation of hMSCs. Finally, we demonstrated that these highly printable NICE bioinks can precisely reconstruct large bone structures reconstructed from CT scans obtained from actual patients. The end goal of this research is to enable patient-specific bioprinting of bone scaffolds to precisely match their injuries. We envision this technique will act as a customizable and easy to work with alternative to autografts that will provide surgeons with greater options for bone surgery.

4. MATERIALS AND METHODS

4.1. Gelatin Methacrylate Synthesis. Gelatin methacrylate was synthesized using porcine gelatin (Bloom no. 300, type A) and methacrylic anhydride, both purchased from Sigma-Aldrich. Eighty percent methacrylated gelatin was created by stirring 10 g of gelatin into 100 mL of phosphate buffered saline (PBS) and allowing to dissolve for 1 h at 60 °C. Eight milliliters of methacrylic anhydride was then added dropwise to the solution over a period of minutes. The solution was maintained at 60 °C for 3 more hours; then, 400 mL of PBS was added. The solution was then dialyzed at approximately 50 °C for 7 days, then lyophilized.

4.2. NICE Bioink Synthesis. κ-Carrageenan was obtained from TCI America, nanosilicates (Laponite XLG) were purchased from BYK Additives, and Irgacure 2959 (2-hydroxy-4′-(2-hydroxyethoxy)-2-methylpropio-phenone) was purchased from Sigma-Aldrich. The NICE bioinks for optimization were created in varying compositions, but the eventual bioink chosen for investigation was composed of 7.5% w/v GelMa, 1% w/v κ-carrageenan, 2% w/v nanosilicates, and 0.25% w/v Irgacure 2959 dissolved in reverse-osmosis purified water. The final concentration was reached by 1:1 mixing of a 15% GelMA, 2% kCA, 0.5% Irgacure 2959 (w/v) solution with a 4% (w/v) Laponite XLG solution. The solution was warmed at 40 °C and stirred continuously overnight to maximize homogeneity. Bioinks were stored refrigerated at 4 °C and warmed to 40 °C before use.

4.3. Three-Dimensional Bioprinter. The bioprinter was created by modifying a commercial ANET A8 3D printer kit to utilize screw extrusion. The thermoplastic extruder assembly was replaced with a 3D printed screw extruder assembly, which holds a stepper motor, guide rail, and a modified clay extruder. Firmware changes were made to accommodate the new extruder motor as needed. All prints used a 400 μm interior diameter tapered extruder tip.

4.4. Three-Dimensional Printing. Deidentified patient data was obtained in the form of DICOM files, which were converted into STL formats. Other printed shapes were created using Solidworks and exported as STL files. STL files were processed in Slic3r Prusa Edition to convert them into G-code printer instructions. Repetier Host was used to control the 3D printer. For printed structures, layer height was 200 μm, line width was 600 μm with a 15% overlap, print speed was 15 mm/s for all trials. The standard 3D printability test was adapted from Chimene 2018: a 10 mm outer diameter hollow cylinder with 1 mm thick walls was printed up to 3 cm (150 layers) in height. Printability performance was quantified by (1) determining whether a composition could reach the full 3 cm height, (2) the absence of major defects by testing whether the cylinder could hold water, and (3) comparing height and diameter of the printed cylinder to its intended dimensions. The prints were also qualitatively evaluated for wall smoothness by examining structures under a stereomicroscope. Bioinks were covalently cross-linked with a 365 nm UV-A light source at 25 mW/cm^2 intensity. Ionic crosslinking was through submersion in a 5% potassium chloride solution.

4.5. Mechanical Testing. Hydrogel samples were printed as cylinders 6 mm in diameter by 2.5 mm thick. Each sample's diameter and height were verified with both digital calipers and the mechanical tester, an ADMET MTEST Quattro eXpert 7600. Any dimensional variations were factored into each sample's stress and strain calculations. Mechanical tests were run as a single cycle unconstrained compression test, where samples were compressed to 30% of their original height over 1 min, then returned back to their original height over another minute. The force and position data recorded by the mechanical tester was analyzed using a custom excel macro to calculate the compressive modulus from 0 to 20% strain, maximum stress, toughness, and energy dissipated.

4.6. Three-Dimensional Bioprinting. Bioprinting was performed using the optimized NICE bioink: deionized (DI) water containing 7.5% w/v GelMA, 1% w/v k-carrageenan, 2% w/v nanosilicates, and 0.25% w/v Irgacure 2959. Primary bone marrow-derived hMSC stem cells were supplied from ATCC. Immediately before bioprinting, cells were trypsinized for 5 min, then 10 mL of media was added, and the resulting cell-media suspension was centrifuged for 5 min. The supernatant was removed, and the cell pellet was resuspended in 200 μL of media, which was gently mixed into the warmed and prepared bioink by pipetting. The bioprinter was moved to a biosafety cabinet and printing proceeded under sterile conditions. Print settings were kept consistent with 3D printability tests described above, using a 200 μm layer height, 600 μm line width with 15% overlap, 15 mm/s print speed, and using a 400 μm tapering luer-lock extruder tip. Other settings were also kept consistent between prints. Covalent cross-linking was carried out after printing was complete, using 25 mW/cm^2 of 365 nm UV-A light for 60 s. Cation content of the media was relied on for ionic cross-linking.[35,36]

Bioprinted scaffolds were printed in several configurations, most often as 1 mm thick, 1 cm diameter disks with 100% infill to allow easy visualization. Crosshatch patterns were also created as 4 cm × 4 cm scaffolds, and the cylindrical printability test cylinder described above was also conducted up to 3 cm in height to verify printability with high layer numbers.

4.7. In Vitro Studies. Bioprinted structures were crosslinked with UV light and incubated in osteoconductive media containing Minimum Essential Media-Alpha Modification (GE Life Sciences) with 16.5% FBS, 1% penicillin-streptomycin, 10 mmol β-glycerophosphate, and 0.05 mmol ascorbic acid. No osteoinductive agents such as dexamethasone or bone morphogenic protein-2 (BMP-2) were added. Media was changed every 3−4 days.

4.8. Degradation Studies. Hydrogel samples were stored in incubator conditions in PBS, media, and media with 300 u/mL of collagenase. Hydrogel mass was taken by removing the hydrogel and all hydrogel pieces large enough to grasp with forceps, dabbing on a Kimwipe to wick away surface liquid, and measuring wet weight using a covered scale and weigh-boat. Mechanical testing was carried out as described above. Time points were taken at days 0, 2, 7, 14, 21, 28, 35, and 60.

4.9. Scanning Electron Microscopy/Energy Dispersive Spectroscopy. For electron microscope imaging and elemental characterization of lyophilized bioink microstructure, an FEI Quanta 600 field emission-scanning electron microscope (FEI-SEM) was used, equipped with an inbuilt Oxford EDS detector with X-ray mapping, and running INCA software. Samples were sputter coated with iridium to a thickness of 8 nm. Voltage was set to 15 kV, and secondary electron mode was used.

4.10. Peak Hold Studies/Shear Recovery Studies. TA rheometer (AR 2) was used for rheology studies, with an 8 mm flat geometry plate, and a gap size of 200 μm. For shear recovery testing, the shear rate was initially held at 0.75 s^{-1} for 60 s at 37 °C; then, the shear rate was increased to 300 s^{-1} for 5 s; then, the shear rate was dropped to 0.2 s^{-1} and temperature was dropped to 25 °C for 180 s.

4.11. Calcium Assay. The calcium content assay experiment was carried out using a Calcium Assay Kit from Cayman Chemical (Item #701220). Bioprinted scaffolds were lyophilized and weighed; then, calcium was dissolved from the scaffold using an HCL solution. Solutions were then diluted with the supplied calcium assay buffer solution and calcium detector reagents were added according to the assay manual. The calcium binds to cresolphthalein complexone to

https://dx.doi.org/10.1021/acsami.9b19037
ACS Appl. Mater. Interfaces XXXX, XXX, XXX−XXX

form a vivid purple complex, which was quantified using a Tecan M200 Pro plate reader and normalized against dilutions of the supplied calcium solution of known concentration.

4.12. RNA-seq Sample Preparation and Analysis. Two biological replicates of hMSCs (one obtained from Lonza Inc and another from Texas A&M Institute for Regenerative Medicine) were used for RNA-seq. hMSCs (2500 cell/cm^2) were cultured in normal media conditions until 65% confluency, then exposed to 50 μg/mL Laponite XLG nanosilicates for 48 h. Cells were then cultured in osteocondictive media for 21 days. Control cells were cultured in osteocondictive media for 21 days in absence of nanosilicates. After 21 days, cells were washed with PBS and pelleted; then, mRNA was collected using a Roche High-Purity RNA Isolation Kit according to the manufacturer's instructions. Nucleic acids were evaluated for quality using a spectrophotometer to analyze absorbance ratios. Initial quality of nucleic material (~1.5−2.0 μg) was evaluated using spectrometer absorbance ratios between 280/260 nm around 2.0. Samples were analyzed via a Illumina NovaSeq 6000 platform with TruSeqRNA sample preparation and paired-end read length of 150 bases (Genomics and Bioinformatics Service, Texas A&M AgriLife Research, College Station, TX). The sequenced reads were aligned to the reference genome (hg38, Genome Reference Consortium Human Build 38 patch release 13 (GRCh38.p13)) using RNA-seq aligner (STAR aligner).[37] Genome browser was utilized for obtaining the gene definition. The gene models can also be obtained by using the Bioconductor package Genomic- Features in R environment. Expression of a gene was determined by counting the number of uniquely mapped reads overlapping the coding exons normalized by gene length in fragments per kilobase per million (FPKM). We utilized the FPKM measure only to filter the expressed genes. The distribution of expression of genes in each sample shows that 1 FPKM is a reasonable cutoff to remove the genes with no or minimal expression. Genes >1 FPKM were considered to be expressed in any condition if they were expressed in both the replicates. Genes expressed in at least one of the condition were then tested for differential expression. The replicates for both the conditions showed high concordance (r = 0.96 for hMSCs and r = 0.98 for hMSCs treated with nanosilicates). We used generalized linear models (GLMs)[38] to identify differentially gene expression (DGE) between nanosilicate treated hMSCs and untreated hMSCs, where the expression counts were modeled as negative binomial distribution. The bioconductor package DESeq was used for this purpose. The gene ontology (GO) enrichment analysis was done using GOStats bioconductor package.[39] Only genes with a P adjusted value (Benjamini−Hochberg false-discovery rate) < 0.05 were included for GO enrichment analysis. All analyses were done in R.

ASSOCIATED CONTENT

Supporting Information

The Supporting Information is available free of charge at https://pubs.acs.org/doi/10.1021/acsami.9b19037.

> Data deposition: The data reported in this paper have been deposited in the Gene Expression Omnibus (GEO) database, https://www.ncbi.nlm.nih.gov/geo (accession no. GSE146309). Dataset S1: Gene expression data (TXT)
>
> Dataset S2: Gene ontology (GO) analysis (TXT)

AUTHOR INFORMATION

Corresponding Author

Akhilesh K. Gaharwar − *Department of Biomedical Engineering, College of Engineering, Department of Material Science and Engineering, College of Engineering, and Center for Remote Health Technologies and Systems, Texas A&M University, College Station, Texas 77843, United States;* orcid.org/0000-0002-0284-0201; Phone: (979) 458-5540; Email: gaharwar@tamu.edu; Fax: (979) 845-4450

Authors

David Chimene − *Department of Biomedical Engineering, College of Engineering, Texas A&M University, College Station, Texas 77843, United States*

Logan Miller − *Department of Biomedical Engineering, College of Engineering, Texas A&M University, College Station, Texas 77843, United States*

Lauren M. Cross − *Department of Biomedical Engineering, College of Engineering, Texas A&M University, College Station, Texas 77843, United States*

Manish K. Jaiswal − *Department of Biomedical Engineering, College of Engineering, Texas A&M University, College Station, Texas 77843, United States*

Irtisha Singh − *Department of Molecular and Cellular Medicine, College of Medicine, Texas A&M Health Science Center, Bryan, Texas 77807, United States;* orcid.org/0000-0002-9460-3587

Complete contact information is available at: https://pubs.acs.org/10.1021/acsami.9b19037

Author Contributions

D.C. and A.K.G. designed the experiments and wrote the manuscript. D.C. and L.M. performed the rheological studies, mechanical characterization, degradation studies, and in vitro cell experiments. M.K.J. performed SEM and EDS. L.M. collected samples for RNA-seq and I.S. analyzed the RNA-seq data. All authors have given approval to the final version of the manuscript.

Funding

A.K.G. would like to acknowledge financial support from the National Institute of Biomedical Imaging and Bioengineering (NIBIB) of the National Institutes of Health (NIH) Director's New Innovator Award (DP2 EB026265), the National Institute of Arthritis and Musculoskeletal and Skin Diseases (NIAMS) award (R21 AR072292) and the National Science Foundation (NSF) Award (CBET 1705852). The content is solely the responsibility of the authors and does not necessarily represent the official views of the funding agency.

Notes

The authors declare no competing financial interest.

REFERENCES

(1) Murphy, S. V.; Atala, A. 3D Bioprinting of Tissues and Organs. *Nat. Biotechnol.* **2014**, *32*, 773.

(2) Kang, H.-W.; Lee, S. J.; Ko, I. K.; Kengla, C.; Yoo, J. J.; Atala, A. A 3D Bioprinting System to Produce Human-scale Tissue Constructs with Structural Integrity. *Nat. Biotechnol.* **2016**, *34*, 312−319.

(3) Moroni, L.; Burdick, J. A.; Highley, C.; Lee, S. J.; Morimoto, Y.; Takeuchi, S.; Yoo, J. J. Biofabrication Strategies for 3D In Vitro Models and Regenerative Medicine. *Nat. Rev. Mater.* **2018**, *3*, 21.

(4) Ashammakhi, N.; Hasan, A.; Kaarela, O.; Byambaa, B.; Sheikhi, A.; Gaharwar, A. K.; Khademhosseini, A. Advancing Frontiers in Bone Bioprinting. *Adv. Healthcare Mater.* **2019**, *8*, No. 1801048.

(5) Kolesky, D. B.; Homan, K. A.; Skylar-Scott, M. A.; Lewis, J. A. Three-dimensional Bioprinting of Thick Vascularized Tissues. *Proc. Natl. Acad. Sci. U.S.A.* **2016**, *113*, 3179−3184.

(6) Chimene, D.; Lennox, K. K.; Kaunas, R. R.; Gaharwar, A. K. Advanced Bioinks for 3D Printing: A Materials Science Perspective. *Ann. Biomed. Eng.* **2016**, *44*, 2090−2102.

(7) Malda, J.; Visser, J.; Melchels, F. P.; Jüngst, T.; Hennink, W. E.; Dhert, W. J. A.; Groll, J.; Hutmacher, D. W. 25th Anniversary Article: Engineering Hydrogels for Biofabrication. *Adv. Mater.* **2013**, *25*, 5011−5028.

(8) Chimene, D.; Peak, C. W.; Gentry, J.; Carrow, J. K.; Cross, L. M.; Mondragon, E.; Cardoso, G. B. C.; Kaunas, R.; Gaharwar, A. K. Nanoengineered Ionic-Covalent Entanglement (NICE) Bioinks for 3D Bioprinting. *ACS Appl. Mater. Interfaces* **2018**, *10*, 9957−9968.

(9) Chimene, D.; Kaunas, R.; Gaharwar, A. K. Hydrogel Bioink Reinforcement for Additive Manufacturing: A Focused Review of Emerging Strategies. *Adv. Mater.* **2020**, *32*, No. 1902026.

(10) Creton, C. 50th Anniversary Perspective: Networks and Gels: Soft but Dynamic and Tough. *Macromolecules* **2017**, *50*, 8297−8316.

(11) Gaharwar, A. K.; Cross, L. M.; Peak, C. W.; Gold, K.; Carrow, J. K.; Brokesh, A.; Singh, K. A. 2D Nanoclay for Biomedical Applications: Regenerative Medicine, Therapeutic Delivery, and Additive Manufacturing. *Adv. Mater.* **2019**, *31*, No. 1900332.

(12) Dawson, J. I.; Oreffo, R. O. Clay: New Opportunities for Tissue Regeneration and Biomaterial Design. *Adv. Mater.* **2013**, *25*, 4069−4086.

(13) Brokesh, A. M.; Gaharwar, A. K. Inorganic Biomaterials for Regenerative Medicine. *ACS Appl. Mater. Interfaces* **2020**, *12*, 5319−5344.

(14) Gaharwar, A. K.; Mihaila, S. M.; Swami, A.; Patel, A.; Sant, S.; Reis, R. L.; Marques, A. P.; Gomes, M. E.; Khademhosseini, A. Bioactive Slicate Nanoplatelets for Osteogenic Differentiation of Human Mesenchymal Stem Cells. *Adv. Mater.* **2013**, *25*, 3329−3336.

(15) Carrow, J. K.; Cross, L. M.; Reese, R. W.; Jaiswal, M. K.; Gregory, C. A.; Kaunas, R.; Singh, I.; Gaharwar, A. K. Widespread Changes in Transcriptome Profile of Human Mesenchymal Stem Cells Induced by Two-dimensional Nanosilicates. *Proc. Natl. Acad. Sci. U.S.A.* **2018**, *115*, E3905−E3913.

(16) Paul, A.; Manoharan, V.; Krafft, D.; Assmann, A.; Uquillas, J. A.; Shin, S. R.; Hasan, A.; Hussain, M. A.; Memic, A.; Gaharwar, A. K.; Khademhosseini, A. Nanoengineered Biomimetic Hydrogels for Guiding Human Stem Cell Osteogenesis in Three Dimensional Microenvironments. *J. Mater. Chem. B* **2016**, *4*, 3544−3554.

(17) Xavier, J. R.; Thakur, T.; Desai, P.; Jaiswal, M. K.; Sears, N.; Cosgriff-Hernandez, E.; Kaunas, R.; Gaharwar, A. K. Bioactive Nanoengineered Hydrogels for Bone Tissue Engineering: A Growth-Factor-Free Approach. *ACS Nano* **2015**, *9*, 3109−3118.

(18) Peak, C. W.; Singh, K. A.; Adlouni, M.; Chen, J.; Gaharwar, A. K. Printing Therapeutic Proteins in 3D using Nanoengineered Bioink to Control and Direct Cell Migration. *Adv. Healthcare Mater.* **2019**, *8*, No. 1801553.

(19) Mouser, V. H.; Melchels, F. P.; Visser, J.; Dhert, W. J.; Gawlitta, D.; Malda, J. Yield Stress Determines Bioprintability of Hydrogels based on Gelatin-methacryloyl and Gellan Gum for Cartilage Bioprinting. *Biofabrication* **2016**, *8*, No. 035003.

(20) Zhang, T.; Lin, S.; Shao, X.; Shi, S.; Zhang, Q.; Xue, C.; Lin, Y.; Zhu, B.; Cai, X. Regulating Osteogenesis and Adipogenesis in Adipose-derived Stem Cells by Controlling Underlying Substrate Stiffness. *J. Cell. Physiol.* **2018**, *233*, 3418−3428.

(21) Steward, A. J.; Kelly, D. J. Mechanical Regulation of Mesenchymal Stem Cell Differentiation. *J. Anat.* **2015**, *227*, 717−731.

(22) Engler, A. J.; Sen, S.; Sweeney, H. L.; Discher, D. E. Matrix Elasticity Directs Stem Cell Lineage Specification. *Cell* **2006**, *126*, 677−689.

(23) Paul, A.; Manoharan, V.; Krafft, D.; Assmann, A.; Uquillas, J. A.; Shin, S. R.; Hasan, A.; Hussain, M. A.; Memic, A.; Gaharwar, A. K.; Khademhosseini, A. Nanoengineered Biomimetic Hydrogels for Guiding Human Stem Cell Osteogenesis in Three Dimensional Microenvironments. *J. Mater. Chem. B* **2016**, *4*, 3544−3554.

(24) Loebel, C.; Mauck, R. L.; Burdick, J. A. Local Nascent Protein Deposition and Remodelling Guide Mesenchymal Stromal Cell Mechanosensing and Fate in Three-dimensional Hydrogels. *Nat. Mater.* **2019**, *18*, No. 883.

(25) Chen, F.-M.; Liu, X. Advancing Biomaterials of Human Origin for Tissue Engineering. *Prog. Polym. Sci.* **2016**, *53*, 86−168.

(26) Loessner, D.; Meinert, C.; Kaemmerer, E.; Martine, L. C.; Yue, K.; Levett, P. A.; Klein, T. J.; Melchels, F. P. W.; Khademhosseini, A.; Hutmacher, D. W. Functionalization, Preparation and Use of Cell-laden Gelatin Methacryloyl−Based Hydrogels as Modular Tissue Culture Platforms. *Nat. Protoc.* **2016**, *11*, 727.

(27) An, Y. H.; Martin, K. L. *Handbook of Histology Methods for Bone and Cartilage*, 2003.

(28) De Godoy, R. F.; Hutchens, S.; Campion, C.; Blunn, G. Silicate-substituted Calcium Phosphate with Enhanced Strut Porosity Stimulates Osteogenic Differentiation of Human Mesenchymal Stem Cells. *J. Mater. Sci.: Mater. Med.* **2015**, *26*, No. 54.

(29) Shendure, J. The Beginning of the End for Microarrays? *Nat. Methods* **2008**, *5*, 585−587.

(30) Cloonan, N.; Forrest, A. R.; Kolle, G.; Gardiner, B. B.; Faulkner, G. J.; Brown, M. K.; Taylor, D. F.; Steptoe, A. L.; Wani, S.; Bethel, G.; Robertson, A. J.; Perkins, A. C.; Bruce, S. J.; Lee, C. C.; Ranade, S. S.; Peckham, H. E.; Manning, J. M.; McKernan, K. J.; Grimmond, S. M. Stem Cell Transcriptome Profiling via Massive-scale mRNA Sequencing. *Nat. Methods* **2008**, *5*, 613−619.

(31) Mortazavi, A.; Williams, B. A.; McCue, K.; Schaeffer, L.; Wold, B. Mapping and Quantifying Mammalian Transcriptomes by RNA-Seq. *Nat. Methods* **2008**, *5*, 621−628.

(32) Rutkovskiy, A.; Stensløkken, K.-O.; Vaage, I. J. Osteoblast Differentiation at a Glance. *Med. Sci. Monit. Basic Res.* **2016**, *22*, 95−106.

(33) Wu, M.; Chen, G.; Li, Y.-P. TGF-β and BMP Signaling in Osteoblast, Skeletal Development, and Bone Formation, Homeostasis and Disease. *Bone Res.* **2016**, *4*, No. 16009.

(34) Bortell, R.; Barone, L. M.; Tassinari, M. S.; Lian, J. B.; Stein, G. S. Gene Expression During Endochondral Bone Development: Evidence for Coordinate Expression of Transforming Growth Factor β1 and Collagen type I. *J. Cell. Biochem.* **1990**, *44*, 81−91.

(35) Mangione, M. R.; Giacomazza, D.; Bulone, D.; Martorana, V.; Cavallaro, G.; San Biagio, P. L. K+ and Na+ Effects on the Gelation Properties of k-Carrageenan. *Biophys. Chem.* **2005**, *113*, 129−135.

(36) Hermansson, A. M.; Eriksson, E.; Jordansson, E. Effects of Potassium, Sodium and Calcium on the Microstructure and Rheological Behaviour of Kappa-carrageenan Gels. *Carbohydr. Polym.* **1991**, *16*, 297−320.

(37) Dobin, A.; Davis, C. A.; Schlesinger, F.; Drenkow, J.; Zaleski, C.; Jha, S.; Batut, P.; Chaisson, M.; Gingeras, T. R. "STAR: ultrafast universal RNA-seq aligner". *Bioinformatics* **2013**, *29* (1), 15−21.

(38) Love, M. I.; Huber, W.; Anders, S. Moderated estimation of fold change and dispersion for RNA-seq data with DESeq2. *Genome Biol.* **2014**, *15*, 550.

(39) Falcon, S.; Gentleman, R. Using GOstats to test gene lists for GO term association. *Bioinformatics* **2007**, *23*, 257−258.